A New Bias Correction Approach for Better Assimilation of Microwave Sounding Data Over Winter Sea Ice in the Korean Integrated Model

Ji-Soo Kim⬤, Myoung-Hwan Ahn⬤, and Sang-Moo Lee, *Member, IEEE*

Abstract— Microwave sounder observations are essential for numerical weather prediction (NWP) systems, but utilizing channels sensitive to surface over sea ice has been challenging due to difficulties in estimating the sea ice surface radiance. This study presents a preprocessing method to assimilate near-surface microwave-sounding observations over winter sea ice, including an estimation of a real-time surface emissivity from satellite radiance and a bias correction scheme to minimize the radiance discrepancy between observation and model simulation. Our results show that the radiance simulated using dynamic emissivity exhibits a much better agreement with the measured one, although a significant negative bias of about 0.61–1.18 K remains over the winter sea ice. Thus, a new bias correction procedure, based on the regression relationships between the residual bias and potential bias sources such as the surface temperature and surface emissivity, is added. When it is applied, the remained bias is successfully estimated. Moreover, the sea ice observations from all temperature-sounding channels have been better utilized in the Korean Integrated Model (KIM). The additional information on the polar regions has increased the analysis increment and reduced the ensemble spread. In addition, a neutral to slightly positive impact on temperature analysis errors in layers sensitive to surface radiance encourages further utilization of microwave sounder data over sea ice.

Index Terms— Bias correction, emitting layer temperature, microwave radiance, sea ice, surface emissivity.

I. INTRODUCTION

MICROWAVE sounder observations play a significant role in improving the forecast skills of numerical weather prediction (NWP) systems, providing information on atmospheric thermodynamic properties (i.e., temperature and humidity) as well as hydrometeor properties [1], [2].

The use of microwave-sounding data is highly dependent on surface types and observation conditions due to varying

microwave radiance emissions associated with different surface types, such as ocean, land, and snow/ice. For instance, the ocean surface, characterized by lower emissivities, exhibits lower surface radiance compared to land or snow/ice surfaces. Utilization of microwave radiances over land and snow/ice has been more challenging than over the ocean, primarily due to the difficulty in the simulation of surface radiances, which is caused by lack of a reliable auxiliary surface information, such as emissivity or temperature [3], [4], [5].

The main problem in the estimation of surface emissivity is the changes in complex dielectric properties which depend on ice age, volume scattering, salinity, and wetness of which basin-scale data are unavailable [6], [7], [8], [9]. Previous studies [10], [11] have focused on enhancing the utilization of microwave observations on all surfaces, primarily by improving the accuracy of microwave surface emissivity [12]. An emissivity model [11], [13] and a method to retrieve the microwave surface emissivity over land and sea ice from passive microwave observations [10], [14], [15], [16], [17], [18], [19], [20] was developed. The observation-based retrieval method has been subsequently incorporated into operational NWP models for assimilating microwave observations over land and sea ice [21], [22], [23], [24], [25], [26]. However, the use of microwave observations over winter sea ice has been challenging due to significant discrepancies in radiances between observation and simulations [27].

Another critical factor in estimating the surface radiances is the accuracy of surface temperature. Sea ice is often covered with snow, and the microwave emitting layer can lie inside the snow layer at microwave frequencies, such as 23.8, 31.4, and 50.3 GHz [28]. Thus, to simulate surface radiance accurately, it is important to consider the temperature of the emitting layer rather than skin temperature. However, it is difficult to estimate the emitting layer temperature due to its dependencies on physical variables such as snow depth on sea ice, and dielectric properties of snow and ice at a certain frequency are difficult to obtain [11].

Studies have been made to estimate the temperature of the emitting layer [23], [29], [30], although these methods are not incorporated in global operational NWP systems because they are confined to specific locations or require additional physical information such as refractivity index or penetration depth or ice types. Instead of emitting layer temperature, the skin temperature from the NWP model is alternatively used as input to simulate background radiances, which can

lead to a biased simulation result specifically at microwave frequencies. The biased data are excluded from assimilation since data assimilation systems are designed to derive solutions using unbiased data [31]. Therefore, an additional correction is necessary to mitigate this bias and to enhance the accuracy of the assimilation results.

The objective of this study is to assimilate microwave radiances at near-surface channels by solving the problem inherent in sea ice emissivity and surface temperature. For better utilization of winter sea ice data, this study investigated the preprocessing methods of a microwave sounder by using emissivity retrieved from the microwave observations and introducing a bias correction scheme to address the uncertainty of surface temperature. For bias correction, this study identified the source of the bias and determined the predictors that can represent the bias.

The remainder of this article is structured as follows. The used observation and model data in this study are described in Section II. The preprocessing methods including characteristics of the dynamically calculated sea ice emissivity and a method to minimize the surface radiance discrepancy between observation and simulation are described in Section III. Further, the microwave-sounding observations over winter sea ice are assimilated in the Korean Integrated Model (KIM) system using the preprocessing methods, and their impacts on the KIM model are analyzed in Section IV. Finally, Section V provides a summary and conclusion of the research.

II. DATA

A. Advanced Technology Microwave Sounder (ATMS)

This study utilizes ATMS observations onboard the Suomi National Polar-orbiting Partnership (SNPP) launched in October 2011 and the National Oceanic and Atmospheric Administration (NOAA)-20 satellite launched in October 2017 as part of the Joint Polar Satellite System (JPSS) series [32]. ATMS is a cross-track scanner with 96 fields of views (FOVs), resulting in varying scan ($\pm$ 53.28°) and polarization angles [33], [34]. It has 22 channels, frequencies from 23 to 183 GHz, including five window channels (i.e., 23.8, 31.4, 50.3, 88.2, and 165.6 GHz), 12 temperature-sounding channels having center frequencies near $\sim$51.76–57.29 GHz, and five humidity sounding channels having center frequencies near $\sim$183 GHz. The radiances at sounding channels are directly assimilated in the NWP models, while the window channels are used for surface emissivity calculation [10], [15] and cloud screening processes [35], [36].

B. KIM Data

For the simulation of the microwave observation radiances, the 6-h forecasting atmospheric and surface state vectors from the KIM system were used. The KIM system has been used as an operational weather forecasting model by the Korean Meteorological Administration (KMA) since 2020 [37]. It produces global-scale analysis and forecasting fields of the atmosphere and the surface variables every 6-h. The model variables are represented in a cubed-sphere grid, having a horizontal resolution of about 12 km and a vertical resolution of 91 levels up to approximately 80 km (i.e., 0.01 hPa) from

the surface. In the KIM system, the initial condition of the model is updated by the Hybrid 4-D Ensemble Variational (H4DEV) method, implementing the local ensemble transform Kalman filter (LETKF) with 50 ensemble members [38], [39], [40]. Various types of observation data, including conventional data and satellite radiances, are assimilated into KIM. The quality of these observations is controlled through a Korean Institute of Atmospheric Prediction Systems (KIAPS) Package of Observation Processing (KPOP) [41]. For the satellite radiance, the quality of bias-corrected observations in clear-sky conditions is evaluated against its model counterpart (i.e., background) simulated from a radiative transfer model for television infrared orbiting satellite (TIROS) operational vertical sounder (TOVS) (RTTOV)-12.3 [42]. For instance, if the difference between observed and background brightness temperatures (TBs) (hereafter, referred to as O−B) is greater than an empirically decided threshold, the observations are not used for data assimilation.

For the microwave sounders, the channels to be assimilated are selected based on the surface types (e.g., ocean, land, sea ice, and snow-covered land). If the land fraction within the model grid is less than 30%, it is classified as ocean. The ocean surface is classified as sea ice when the sea ice concentration, from Operational Sea Surface Temperature and Ice Analysis (OSTIA) [43], is greater than or equal to 20%. Finally, if the surface snow amount (e.g., snow water equivalent) is greater than or equal to 1.0 kg/m^2, it is classified as snow-covered land. Over the ocean surface, both the temperature and humidity-sounding channels are assimilated. While over the sea ice, the lower tropospheric temperature channels (i.e., ATMS channels 6 and 7 having the peaks of weighting function at 700 and 400 hPa, respectively) and humidity channels are not used because of the large uncertainty in the simulated radiances.

C. Evaluation Data

For the evaluation of analysis fields, the Integrated Forecast System (IFS), which is the operational NWP system of the European Centre for Medium-Range Weather Forecasts (ECMWF), is used. It has the leading forecasting skills among the World Meteorological Organization (WMO) designated meteorological centers [44] and it is widely used as reference data. The resolution of the operational global system is from 18 to 9 km horizontally and 137 model levels.

In addition, the analysis fields were evaluated against the satellite observation, Advanced Microwave Sounder Unit (AMSU)-A observations onboard the NOAA and MetOp European Meteorological Satellite series [45]. It is a cross-track scanner with scan angles within $\pm$49.44° and has 15 channels with frequencies that correspond to those of ATMS channels 1–3 and 5–16.

III. PREPROCESSING METHOD

This section presents a preprocessing method for ATMS temperature channels over winter sea ice. This study focuses on ATMS channels 6 and 7, which are not utilized in the operational KIM system over sea ice. In addition, ATMS channel 5 is analyzed as they can be used for quality control (QC) of ATMS channels 6 and 7 observations over sea ice [27].

A. Dynamic Emissivity of Sea Ice

Here, sea ice emissivity is dynamically derived for each ATMS FOV using the ATMS measurements and KIM data along with the radiative transfer model (RTM). The equation to calculate the surface emissivity is derived from the radiative transfer equation under nonscattering atmosphere conditions.

For microwave frequencies, where the Rayleigh–Jeans approximation is applicable, the radiance is linear with the TB. Thus, the upwelling TB at the top of the atmosphere (TOA) (e.g., TB^{TOA}) is represented by the sum of surface emitted TB, atmospheric upwelling TB (e.g., $\text{TB}^{\uparrow}$), and atmospheric downwelling TB ($\text{TB}^{\downarrow}$) reflected by the surface [15], [17]. The observed p-polarized TB at the frequency ν is expressed as

$$\text{TB}^{\text{TOA}}_{\nu,p} = \varepsilon_{\nu,p} T_{\text{surf}} \tilde{\tau}_\nu + \text{TB}^{\uparrow}_\nu + \text{TB}^{\downarrow}_\nu \left(1 - \varepsilon_{\nu,p}\right) \tilde{T}_\nu \qquad (1)$$

where, $\tilde{T}$ is atmospheric total transmittance and T_{surf} represents the surface temperature, which indicates the surface skin temperature rather than the emitting layer temperature. The implications of using the skin temperature will be discussed in Section III-C. Hereafter, the use of the subscript p will be omitted for simplicity. The ε is the surface emissivity which can be obtained by rearranging (1), as the following:

$$\varepsilon_\nu = \frac{\text{TB}^{\text{TOA}}_\nu - \text{TB}^{\uparrow}_\nu - \text{TB}^{\downarrow}_\nu \tilde{T}_\nu}{\left(T_{\text{surf}} - \text{TB}^{\downarrow}_\nu\right) \tilde{T}_\nu}. \qquad (2)$$

Thus, ε_ν can be estimated by using the measured $\text{TB}^{\text{TOA}}_\nu$ with the auxiliary data, such as $\text{TB}^{\uparrow}_\nu$, $\text{TB}^{\downarrow}_\nu$, and $\tilde{T}_\nu$. Here, $\text{TB}^{\text{TOA}}_\nu$ can be represented by the polarized ATMS observation, allowing the estimated emissivity to account for the variations in the polarization angle. T_{surf} is from the skin temperature from the KIM model. Diurnal variations in skin temperature can have an impact on emissivity estimation results and may also influence bias characteristics. However, during the research period, the diurnal variation in skin temperature was not observed, likely due to the absence of direct solar radiation. Therefore, this study did not consider the diurnal variations in skin temperature. $\text{TB}^{\uparrow}_\nu$, $\text{TB}^{\downarrow}_\nu$, and $\tilde{T}_\nu$ are simulated from the RTTOV-11.2 with forecast fields of the KIM model assuming the specular reflection. While this study did not cover the application of Lambertian reflection, utilizing Lambertian or semi-Lambertian assumptions would enhance the accuracy of microwave radiance simulation, particularly over snow and sea ice surfaces [46], [47]. Thus, the emissivity calculated given by (2) (hereafter, referred to as dynamic emissivity) is an apparent emissivity rather than physical emissivity.

The dynamic emissivities can be calculated from the window channel measurements to minimize the influence of atmospheric radiance. Surface emissivity calculated at 50.3 GHz (i.e., the closest frequency to the temperature sounding channels) can be used to simulate the background TBs of adjacent temperature channels (52.8–57.29 GHz). This is based on the assumption that surface emissivity is constant at frequencies from 50 to 60 GHz [22], which is supported by the stable dielectric constant at this frequency range [48]. Cloud screening was not performed, since the presence of clouds or rain/snow affecting microwave signals at 50–60 GHz constitutes a minority of data during the Arctic winter, although
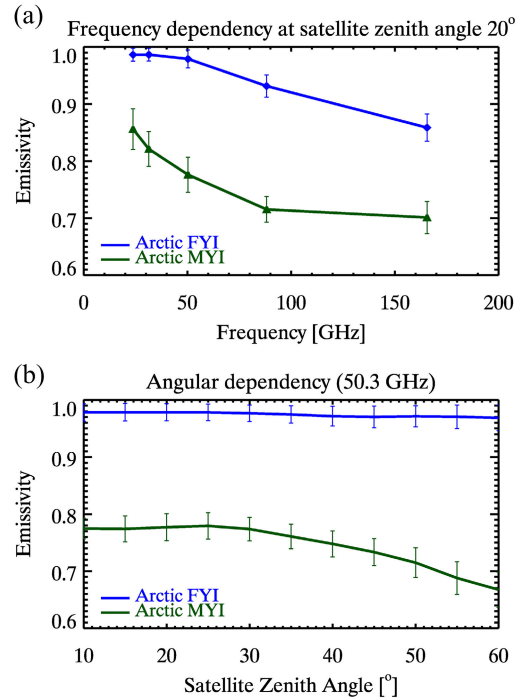

Fig. 1. (a) Frequency and (b) angle dependencies of the dynamic emissivity in the specific areas of winter sea ice: Arctic FYI (blue) and MYI (green). The vertical line represents the standard deviation. For the frequency dependency, the data with satellite zenith angle ranges 10°–20° was used.

these signals are not negligible [49], [50]. To avoid signal contamination from the ocean, the data were used only if the collocated OSTIA sea ice concentration exceeded 95%.

The frequency and angle dependences of dynamic emissivity derived for a 15-day period in January 2022 are shown in Fig. 1 over selected areas in the Arctic, first-year ice (FYI) region (75°N–80°N and 75°E–80°E, the Kara Sea), and multiyear ice (MYI) region (83°N–86°N and 30°W–36°W, north of Greenland). Fig. 1 shows that the dynamic emissivity of MYI is lower than that of FYI due to the larger volume scattering of MYI [51]. In Fig. 1(a), they decrease with increasing frequency since volume scattering is stronger at higher frequencies (i.e., shorter wavelength). Fig. 1(b) shows that the emissivity variation is stable for low satellite zenith angles but decreases at large angles (i.e., 30° and above), especially for MYI, and the decreasing slope is steeper at angles above 50°. Thus, the data with satellite zenith angles above 50° were not used in this study. The frequency and angular behavior of dynamic emissivities agree well with in situ observations as well as theoretically calculated sea ice emissivities [10], [30].

B. TB Simulation Using Dynamic Emissivity

The background TBs at ATMS temperature channels 5–7 were simulated with dynamic emissivity derived at 50.3 GHz. Fig. 2 presents a comparison between the background TB with the observed TB over the winter Arctic Sea ice region. Here, the scan-dependent bias was corrected using static coefficients. Both correlation coefficients and regression slopes are close to 1 for all three channels. However, the biases (mean of
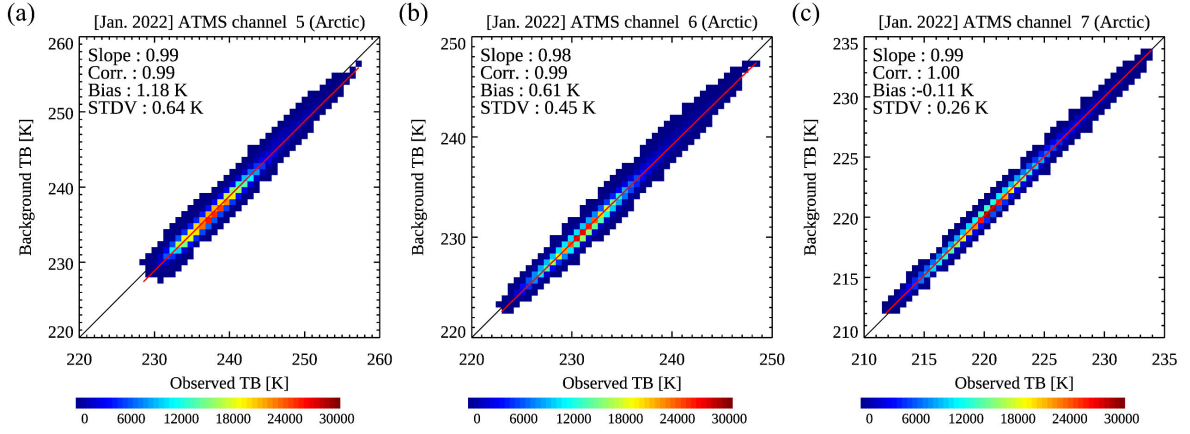
Fig. 2. Density scatter plot between observation and background TB at ATMS channels (a) 5, (b) 6, and (c) 7. The background TB was simulated using the dynamic emissivity at 50.3 GHz. The one-to-one line and regression lines are shown in black and red, respectively.

O–B) at channels 5–6 (1.18 and 0.61 K, respectively) were significant compared to those calculated over the ocean using the FASTEM version 6 emissivities, which yielded values of 0.03 and 0.38 K, respectively. In contrast, the bias at channel 7 was minimal in both sea ice (−0.11 K) and ocean (0.05 K). The significant biases at channels 5 and 6 suggest the need for an additional correction method to remove the bias for better utilization of these data.

Sections III-C and III-D provides the causes of bias that are found exclusively in the winter sea ice regions for ATMS channels 5 and 6, and further describe a method to minimize this bias.

C. TB Sensitivity to Uncertainties in Contributing Variables

In (1), the TB_ν^{TOA} is determined by the variables including surface temperature, emissivity, atmospheric TBs, and transmittance. To better understand potential error sources responsible for the O–B bias, sensitivities of the simulated TBs to uncertainties of the contributing variables (i.e., ε_ν, T_{surf}, $TB_\nu^\uparrow$, $TB_\nu^\downarrow$, and $\tilde{T}_\nu$) are evaluated. Based on a Gaussian error propagation approach, the total variation of TB (ΔTB_ν^{TOA}) due to uncertainties in all contributing variables (V) can be calculated by summing the TB variation for each uncertain variable (i.e., $\left|(\partial TB_\nu^{TOA}/\partial V)\right|\Delta V$), which are estimated by the increment or uncertainty of the variable (ΔV) and the partial derivative of TB (i.e., $(\partial TB_\nu^{TOA}/\partial V)$). It is important to note that this method assumes that variables are independent of each other and that the changes in the variables are small enough to be approximated by their first-order partial derivatives

$$
\begin{aligned}
\Delta TB_\nu^{TOA} &= \left|\frac{\partial TB_\nu^{TOA}}{\partial \varepsilon_\nu}\right|\Delta\varepsilon_\nu + \left|\frac{\partial TB_\nu^{TOA}}{\partial T_{surf}}\right|\Delta T_{surf} + \left|\frac{\partial TB_\nu^{TOA}}{\partial TB_\nu^\uparrow}\right|\Delta TB_\nu^\uparrow \\
&+ \left|\frac{\partial TB_\nu^{TOA}}{\partial TB_\nu^\downarrow}\right|\Delta TB_\nu^\downarrow + \left|\frac{\partial TB_\nu^{TOA}}{\partial \tilde{T}_\nu}\right|\Delta\tilde{T}_\nu.
\end{aligned} \tag{3}
$$

The sensitivity of TB to the contributing variables ($(\partial TB_\nu^{TOA}/\partial V)$) can be mathematically formulated as the following and they were estimated using the 15 days of ATMS

and KIM forecasting data over winter sea ice in January 2022

$$
\frac{\partial TB_\nu^{TOA}}{\partial \varepsilon_\nu} = \left(T_{surf} - TB_\nu^\downarrow\right)\tilde{T}_\nu \tag{4a}
$$

$$
\frac{\partial TB_\nu^{TOA}}{\partial T_{surf}} = \varepsilon_\nu\tilde{T}_\nu \tag{4b}
$$

$$
\frac{\partial TB_\nu^{TOA}}{\partial TB_\nu^\uparrow} = 1 \tag{4c}
$$

$$
\frac{\partial TB_\nu^{TOA}}{\partial TB_\nu^\downarrow} = (1 - \varepsilon_\nu)\tilde{T}_\nu \tag{4d}
$$

$$
\frac{\partial TB_\nu^{TOA}}{\partial \tilde{T}_\nu} = \varepsilon_\nu T_{surf} + TB_\nu^\downarrow(1 - \varepsilon_\nu). \tag{4e}
$$

The uncertainties of the atmospheric variables (i.e., $TB_\nu^\uparrow$, $TB_\nu^\downarrow$, and $\tilde{T}_\nu$) are determined by the accuracy of the RTTOV model and the input data (i.e., atmospheric temperature and humidity profiles). Here, it is assumed that the RTTOV model is sufficiently accurate [52] so that the uncertainty propagated from the input parameters was only examined. Thus, $\Delta TB_\nu^\uparrow$, $\Delta TB_\nu^\downarrow$, and $\Delta\tilde{T}$ were estimated by the changes in these variables with and without errors in temperature and humidity profiles, that were represented by the background error covariance matrix of KIM.

The uncertainty in the surface temperature is mainly caused by the use of skin temperature from KIM rather than the actual emitting layer temperature. The difference between skin temperature and emitting layer temperature is relatively small in the ocean and summer sea ice [23]. In winter sea ice, however, the difference becomes larger because microwave penetration depth becomes deeper and the temperature gradient becomes steeper and it can be as much as 20 K [18], [23], [30]. Thus, for the sensitivity test, the uncertainty of T_{surf} was empirically selected as 20 K.

Here, the dynamic emissivity is considered as independent retrieval and $\Delta\varepsilon$ indicates the uncertainties in the calculation process, which is propagated from the errors in observed TB at window frequencies, $TB_{window}^\uparrow$, $TB_{window}^\downarrow$, $\tilde{T}_{window}$, and T_{surf}. The uncertainty of the observed TB was determined from the reported NEdT values [34] and the chosen error in surface
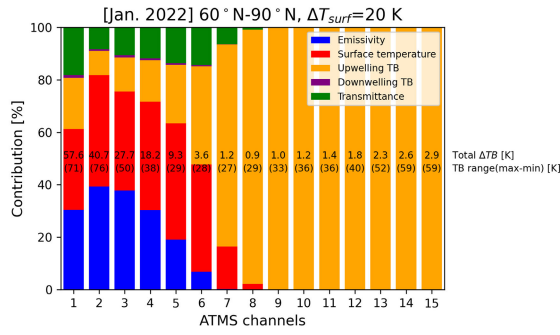
Fig. 3. Percent contribution of uncertainty in variables to the total TB variation at ATMS temperature sounding channels: emissivity (blue), skin temperature (red), upwelling TB (orange), downwelling TB (purple), and atmospheric transmittance (green). The total TB variation and the average TB range are indicated as text within the graph.

temperature (i.e., 20 K) was used. For $\mathrm{TB}^{\uparrow}_{\mathrm{window}}$, $\mathrm{TB}^{\downarrow}_{\mathrm{window}}$, and $\tilde{T}_{\mathrm{window}}$, perturbations were given to the atmospheric profiles, as mentioned earlier. As a result, the uncertainty in 50.3 GHz dynamic emissivity, which is applied to the temperature channels, was estimated to be 0.13.

Next, the variations of TB at the ATMS window and temperature channels due to uncertainty in the variables (i.e., $\left|(\partial\mathrm{TB}^{\mathrm{TOA}}_{v}/\partial V)\right|\Delta V$), while other variables unchanged, were estimated. The contributions of variable uncertainties to the total variability of TB are shown in Fig. 3, illustrating the impact of these variables on TB variation. The TB variations at channels 1–6 are mainly affected by uncertainty in surface temperature. The second largest contributor to channels 1–4 is the uncertainty in dynamic emissivity of which impact on TBs decreases as transmittance decreases. At channels 5 and 6, the contribution of atmospheric upwelling TB exceeds that of surface emissivity, and the impact of emissivity on TB becomes negligible at channels 7–15. Further, at channels 8–15, the TB variations due to the uncertainty in surface temperature become negligible and the corresponding uncertainties in upwelling radiances become the major contributor.

The significant contribution of atmospheric upwelling TB to the TB variation at ATMS channels 8–15 is addressed by implementing scan and air-mass bias correction methods in the operational KPOP system [41]. However, the impact of surface components, such as surface temperature and emissivity, is not considered in the operational system. Thus, this study has developed a new bias correction scheme that can account for the contribution of surface variables and it is described in Section III-D.

D. Bias Correction Method

According to the sensitivity test in Section III-C, it was found that discrepancies in surface emissivity and/or surface temperature and/or upwelling TB between the observation and model spaces could introduce bias in the TB at ATMS channels 5 and 6. Therefore, in this study, the differences in these variables are considered for bias prediction at these channels while disregarding the discrepancies in downwelling TB and transmittance. Then, the microwave radiative transfer equation for observed TB ($\mathrm{TB}^{\mathrm{obs}}_{v}$) and simulated TB ($\mathrm{TB}^{\mathrm{bgr}}_{v}$) are

as the following:

$$\mathrm{TB}^{\mathrm{obs}}_{v} = \varepsilon_v T_{\mathrm{emit}}\tilde{T}_v + \mathrm{TB}^{\uparrow}_{o,v} + \mathrm{TB}^{\downarrow}_{v}(1 - \varepsilon_v)\tilde{T}_v \qquad (5)$$

$$\mathrm{TB}^{\mathrm{bgr}}_{v} = \varepsilon_{d,50.3} T_{\mathrm{skin}}\tilde{T}_v + \mathrm{TB}^{\uparrow}_{b,v} + \mathrm{TB}^{\downarrow}_{v}\left(1 - \varepsilon_{d,50.3}\right)\tilde{T}_v \qquad (6)$$

where, T_{emit} and T_{skin} are the emitting layer and skin temperatures, and ε_v and $\varepsilon_{d,50.3}$ are the real emissivity and dynamic emissivity calculated from the (2), respectively. $\mathrm{TB}^{\uparrow}_{o,v}$ represents atmospheric upwelling TB contributing to $\mathrm{TB}^{\mathrm{obs}}$, while $\mathrm{TB}^{\uparrow}_{b,v}$ represents simulated atmospheric upwelling TBs. Then, the difference in TB between observation and background is

$$\mathrm{TB}^{\mathrm{obs}}_{v} - \mathrm{TB}^{\mathrm{bgr}}_{v}$$
$$= \left(\varepsilon_v T_{\mathrm{emit}} - \varepsilon_{d,50.3}T_{\mathrm{skin}}\right)$$
$$- \mathrm{TB}^{\downarrow}_{v}\left(\varepsilon_v - \varepsilon_{d,50.3}\right)\tilde{T}_v + \left(\mathrm{TB}^{\uparrow}_{o,v} - \mathrm{TB}^{\uparrow}_{b,v}\right). \qquad (7)$$

Let the systematic biases of surface emissivity, surface temperature, and atmospheric upwelling TB be $\Delta\varepsilon_v = \varepsilon_v - \varepsilon_{d,50.3}$, $\Delta T_{\mathrm{surf}} = T_{\mathrm{emit}} - T_{\mathrm{skin}}$, and $\Delta\mathrm{TB}^{\uparrow}_v = \mathrm{TB}^{\uparrow}_{o,v} - TB^{\uparrow}_{b,v}$, respectively. In this study, these terms are considered as constant representing the general state of sea ice based on substantial data. Then, (7) becomes

$$\mathrm{TB}^{\mathrm{obs}}_{v} - \mathrm{TB}^{\mathrm{bgr}}_{v} = \left(T_{\mathrm{skin}} - \mathrm{TB}^{\downarrow}_{v}\right)\tilde{T}_v\Delta\varepsilon_v + \varepsilon_{d,50.3}\tilde{T}_v\Delta T_{\mathrm{surf}}$$
$$+ \tilde{T}_v\Delta\varepsilon_v\Delta T_{\mathrm{surf}} + \Delta\mathrm{TB}^{\uparrow}_v. \qquad (8)$$

Fig. 4 shows the relationship between the terms of $\left(T_{\mathrm{skin}} - \mathrm{TB}^{\downarrow}_{v}\right)\tilde{T}_v$, $\varepsilon_{a,50.3}\tilde{T}_v$, and $\tilde{T}_v$ in (8) and $\mathrm{TB}^{\mathrm{obs}}_{v} - \mathrm{TB}^{\mathrm{bgr}}_{v}$ (O−Bn). It illustrates a linear trend where O−B biases increase as predictor values increase. Data points with high density are closely adhering to the linear regression lines, while those deviating from the regression lines constitute a minority within the dataset. Then, the O−B can be expressed as the multilinear regression equation as the following:

$$\mathrm{TB}^{\mathrm{obs}}_{v} - \mathrm{TB}^{\mathrm{bgr}}_{v} = \sum_{i=1}^{3} P_{i,v}C_{i,v} + C_{4,v} \qquad (9)$$

where $P_{i,v}$ and $C_{i,v}$ represent the predictors and regression coefficients at frequency v. It is noted that $P_{1,v}$, $P_{2,v}$, and $P_{3,v}$ correspond to $\left(T_{\mathrm{skin}} - \mathrm{TB}^{\downarrow}_{v}\right)\tilde{T}_v$, $\varepsilon_{d,50.3}\tilde{T}_v$, and $\tilde{T}_v$, respectively, and $C_{1,v}$, $C_{2,v}$, and $C_{3,v}$ correspond to $\Delta\varepsilon_v$, ΔT_{surf}, and $\Delta\varepsilon_v\Delta T_{\mathrm{surf}}$, respectively. The coefficient $C_{4,v}$ corresponds to $\Delta\mathrm{TB}^{\uparrow}_v$ and the residual bias. Then, the regression coefficients were computed by solving the (9) with the predictors using the winter sea ice data of 15 days in January 2022.

Table I shows the calculated regression coefficients from (9). The positive signs of $C_{2,v}$ and $C_{3,v}$ correspond to the relationship between O–B and $P_{2,v}$, and $P_{3,v}$ shown in Fig. 4(c)–(f), indicating that the O–B values increase with increasing predictor values. However, the negative sign of $C_{1,v}$ contrasts with the O–B dependence on $P_{1,v}$ shown in Fig. 4(a) and (b). This is due to an intercorrelation among the predictors because predictors considered in this study share the $\tilde{T}_v$. Although the intercorrelation between predictors is generally avoided in regression analysis because of the difficulty in interpreting regression coefficients, it can be acceptable, specifically when the predictors hold theoretical significance [53], [54]. In this study, the predictors were selected based on the sensitivity test (see Section III-C) and derived from the microwave
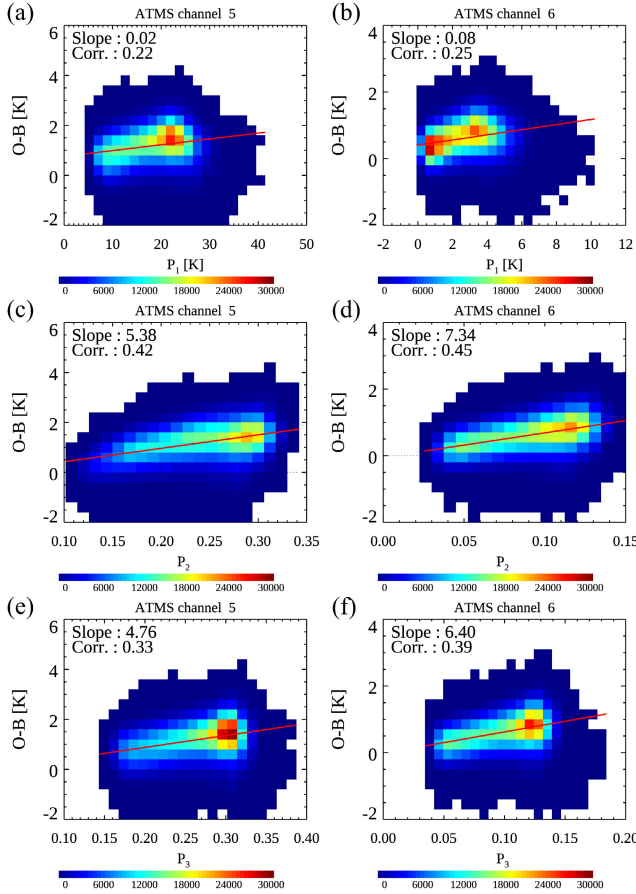
Fig. 4. Density scatter plot between O–B and (a) and (b) P_1, $\left(\left(T_{\text{skin}} - \text{TB}_\nu^\downarrow\right)\tilde{T}_\nu\right)$, (c) and (d) P_2 ($\varepsilon_{d,50.3}\tilde{T}_\nu$), and (e) and (f) $P_3(\tilde{T}_\nu)$ at (left) ATMS channel 5 and (right) ATMS channel 6. The regression lines are represented in red.

TABLE I
BIAS CORRECTION COEFFICIENTS CALCULATED USING THE 15-DAY
DATA FROM 1. JANUARY 2022

Channel	C_1	C_2	C_3	C_4
5	-0.24	7.90	28.46	-3.84
6	-0.33	14.83	9.12	-0.73

radiative transfer equation, providing meaningful insights into the relationship. Thus, the predictors, representing sensitivity in TB to the emissivity, surface temperature, and upwelling TB were employed to represent the O–B bias.

Fig. 5 illustrates the effectiveness of these predictors in bias estimation by comparing the estimated bias with the actual O–B bias at channels 5 and 6, using the same data employed for the multilinear regression analysis. The majority of the data align closely with the one-to-one line, indicating accurate bias estimation. However, the lower slopes (0.42 at channel 5 and 0.34 at channel 6) reflect some data points deviating from the one-to-one line and the presence of inherent uncertainties in the estimation. Notably, these deviating data points constitute a minority of the overall dataset. The potential sources of uncertainties in the bias estimation include neglecting uncertainties in downwelling atmospheric TB and transmittance. In addition, uncertainties may arise in the sea ice conditions that cannot be
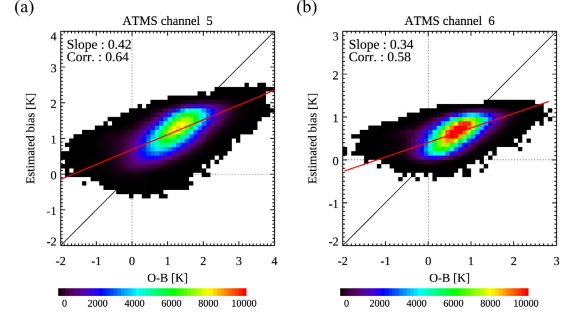

Fig. 5. Density scatter plot between actual O–B and estimated bias using the coefficients shown in Table I for ATMS channels (a) 5 and (b) 6. The regression lines are represented in red.
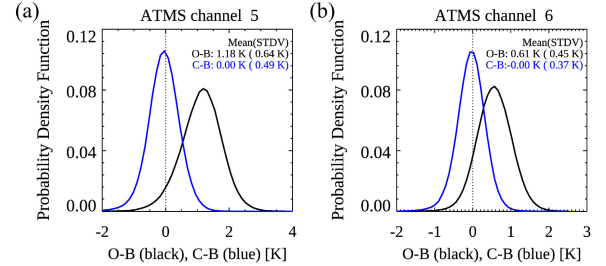

Fig. 6. Histogram of the difference in TB between observation and background at ATMS channels (a) 5 and (b) 6. The differences before bias correction (O–B) are represented in black, while the differences after bias correction (C–B) are represented in blue.
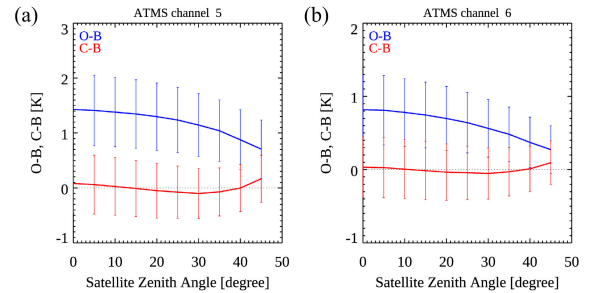

Fig. 7. Angle dependency of the O–B (blue) and C–B (red) bias at (a) ATMS channel 5 and (b) ATMS channel 6. The vertical line represents the standard deviation.

fully accounted for by the regression coefficients, which are susceptible to changes in ice thickness, surface temperature, and emissivities. Any estimation errors would be represented as residual bias after the bias correction.

The bias was corrected by simply subtracting the estimated bias from the O–B values. The mean differences in TBs between bias-corrected observation and background (hereafter, referred to as C–B) were reduced to 0.00 K at both ATMS channels 5 and 6 (original biases were 1.18 and 0.61 K, respectively) (see Fig. 6). Also, the standard deviation was reduced to 0.49 K at channel 5 and 0.37 K at channel 6 (original standard deviations were 0.64 and 0.45 K, respectively).

Furthermore, the angle dependence of O–B and C–B biases was analyzed in Fig. 7. The O–B bias exhibited slightly higher values near the nadir, where the atmosphere is more transparent and thus more sensitive to the surface radiance, compared to the scan edge. However, the C–B biases did not show any significant dependency on scan angles. These

findings suggest that the bias correction was effective across all satellite zenith angles and underscore that the primary contributor to the O–B bias is related to surface radiance.

As a result, the calculated regression coefficients in this study effectively eliminated the biases in winter sea ice, enabling the better utilization of the near-surface ATMS channels in the KIM system.

IV. DATA ASSIMILATION EXPERIMENT

A. Experimental Design

The preprocessing methods described in Section III were applied to the KIM system to assimilate ATMS channels 6 and 7 over Arctic winter sea ice. To evaluate the impact of additionally assimilated observations on the data assimilation process, two experiments were conducted for 45 days from 15 December 2021 to 31 January 2022. Assimilation experiments include a control system (CTRL) that has the same configuration as the operational KIM 3.7a system and an experiment (SeaIceEXP) that assimilates ATMS channels 6 and 7 radiances over sea ice. In both experiments, the spatial resolution of the used model was reduced to 25 km to save the computational cost. In the SeaIceEXP, a cycling experiment was not carried out and the same first guess (FG) as the CTRL system was employed while the analysis and forecasts were regularly updated. This approach was adopted because the skill of NWP models strongly relies on the accuracy of the initial conditions which is provided by the data assimilation system [38]. The key differences between SeaIceEXP and CTRL are in the use of dynamic emissivity and the additional use of ATMS channels 6 and 7 over winter sea ice (the observations over the summer sea ice were not assimilated due to the greater complexity of physical characteristics). In this study, TB at channel 5 was not assimilated, but rather used for QC of ATMS observations over sea ice to mitigate the uncertainties in estimation. In the QC process, the ATMS channels 6 and 7 observations were rejected from the assimilation when 1), the absolute value of bias-corrected O−B at channel 5 was greater than 0.7 K [27] and/or 2), the OSTIA sea ice concentration was lower than 95% and/or 3), and the satellite zenith angle is greater than 50°.

As the bias at ATMS channel 7 is negligible [see Fig. 2(c)] and depends more on the upwelling TB than on the skin temperature (see Fig. 3), an operational scan and air mass predictors for bias correction were utilized [41], [55]. On the other hand, the biases at ATMS channels 5 and 6 were corrected using the bias correction method discussed in Section III-D. Here, the static regression coefficients, which are presented in Table I, were used, while operational scan and air mass predictors were calculated every 6 h. Fig. 8 shows the scatter plot that illustrates the relationship during the experimental period between the O−B and the biases estimated using the precalculated static coefficients. It demonstrates that the estimated biases closely align with the one-to-one line, exhibiting a slope of 0.56 and a correlation coefficient of 0.72. This supports the effectiveness of the static coefficients in estimating the O–B bias during the experimental period within the KIM system.
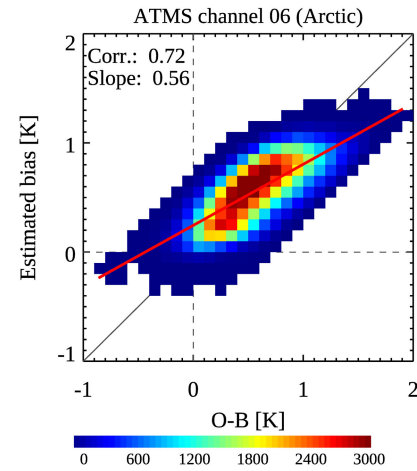

Fig. 8. Density scatter plot of O−B at channel 6 and bias estimated with the static coefficients during the 45 days from December 15, 2021. The one-to-one line and regression lines are shown in black and red solid lines, respectively.
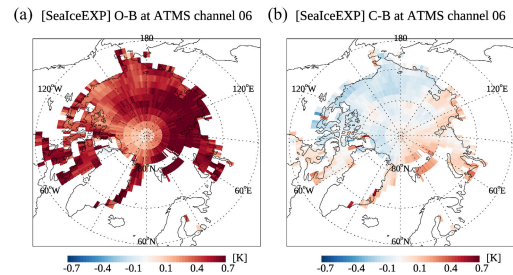

Fig. 9. The 45-day mean distribution of the O–B at ATMS channel 6 before and after bias correction in (a) and (b) over sea ice, respectively.

B. Impact on the QC

Incorporating additional satellite radiance data or modifying the QC process would have a significant impact on the solution of data assimilation (i.e., analysis). Hence, it is necessary to evaluate the impact of SeaIceEXP on the QC and analysis fields by comparing it with the CTRL.

As a result of SeaIceEXP, the number of assimilated ATMS observations at channels 6 and 7 increased by 6% globally compared to the CTRL. In addition, the utilization of ATMS observations at channels 8–15 has increased by 7% globally and 14% specifically over sea ice, as a consequence of the data thinning process. The 45-day averaged spatial distribution of the assimilated observations at ATMS channel 6 over sea ice is shown in Fig. 9. The spatial distribution was obtained by remapping the O–B values into 0.25° by 0.25° grids because the measurement granules of ATMS observation are not regularly distributed. In general, it exhibits positive O−B, with a mean of 0.43 K and a standard deviation of 0.34 K [see Fig. 9(a)]. To remove this bias, the bias in each pixel was estimated using the precalculated static coefficients along with the real-time predictors. After the bias correction, the C–B reduced with a mean of −0.01 K and a standard deviation of 0.21 K [see Fig. 9(b)]. Here, the C–B are positive in the Atlantic Sector and negative in the Pacific/Canadian Sector. Consequently, the bias-corrected observations that passed the
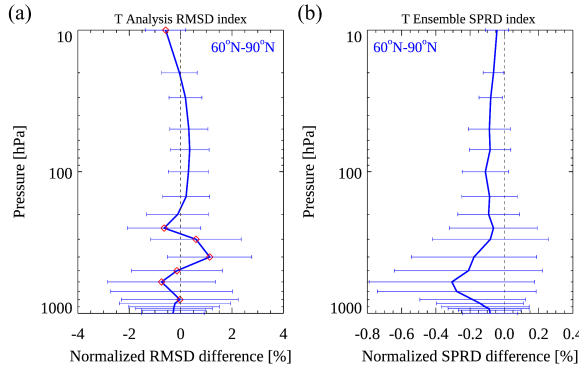
(a)

Fig. 10. Normalized (a) analysis RMSD index and (b) ensemble SPRD index differences (SeaIceEXP minus CTRL) at 25 levels. The levels where the significance level is above 95% is represented by diamond symbols and the horizontal lines represent standard deviations.

QC procedures including thinning were incorporated into the data assimilation system.

C. Impacts on Analysis Fields

The updated model temperature fields as a result of the assimilation of temperature channels were examined against those from the ECMWF IFS system. For the comparison, the atmospheric temperatures were remapped onto 0.25° horizontal grids and 25 vertical levels ranging from 1000 to 1 hPa (vertical levels were selected to align with the isobaric level (ISBL) data formats [56]).

In this study, an index was defined to evaluate the root mean square difference (RMSD) of model analysis in the high-latitude regions. The RMSD index was calculated as below

$$\text{RMSD index} = \frac{\sum_{\theta=60°\text{N}}^{\theta=90°\text{N}} \text{ZM\_RMSD}_\theta \cos\theta}{\sum_{\theta=60°\text{N}}^{\theta=90°\text{N}} \cos\theta}. \quad (10)$$

The index represents the averaged zonal mean of analysis RMSD (ZM_RMSD) in the high latitude regions (above 60°N), where the latitude band (θ) is defined at 0.25° intervals. To account for the decreasing grid area with increasing latitude, ZM_RMSD at each latitude band is normalized by the cosine function. Fig. 10(a) shows the normalized difference in the RMSD index for temperature between CTRL and SeaIceEXP and a statistically significance level above 95% is marked as red. Here, a negative value indicates that the RMSD of SeaIceEXP is smaller than that of CTRL.

At the levels from surface to 500 hPa, which corresponds to the weighting function of ATMS channel 6, the RMSD decreased with significance levels above 95% as a result of SeaIceEXP. The evaluation results of temperature analysis and background fields at 700 hPa, where the peak of the weighting function of ATMS channel 6 is located, are shown in Fig. 11(a), (c), (e), and (g). In the 700 hPa background field, the temperature of KIM has a warm bias in the Pacific/Canadian Sector and a cold bias in the Atlantic Sector [see Fig. 11(a)] compared to that of IFS. Fig. 11(c) and (e) show the analysis increment of CTRL and SeaIce-EXP, respectively. The increment was negligible in CTRL while SeaIceEXP exhibits a greater magnitude than CTRL.

As expected, the direction of the analysis increment corresponds to the distribution of the C–B of ATMS channel 6 [see Fig. 9(b)]. The positive increment was found in the Atlantic Sector where the cold bias of temperature background was exhibited, while the negative increment was given to the Pacific/Canadian Sector where the warm bias of temperature background was exhibited. As a result, the RMSDs decreased by 0.2 K ($\sim$1%) in the Chukchi and East Siberian Seas [see Fig. 11(g)]. However, an increase in the RMSD was found in the Central Arctic Seas (near 30°E) due to the larger C–B values in this area compared to the surroundings [see Fig. 9(b)], resulting in a large increment. This issue can be addressed by adjusting error covariances or implementing stricter QC thresholds.

At 300–400 hPa, which corresponds to the weighting function of ATMS channel 7, the RMSD index increased and the significance level was above 95%. The evaluation results of temperature background and analysis fields at 400 hPa are shown in Fig. 11(b), (d), (f), and (h). The atmospheric temperature at 400 hPa of the KIM background was colder than that of IFS across the entire Arctic Ocean [see Fig. 11(b)] and the analysis increment of SeaIceEXP was given to increase the RMSD at the central Arctic Ocean [see Fig. 11(f)]. The spatial distribution of analysis increment is consistent with the FG-departures of ATMS channel 7 (not shown). The C–Bs of ATMS channel 7 exhibited negative values over the sea ice, suggesting that there may be a need to improve the quality of channel 7 observation to enhance the accuracy of analysis fields. Although the negative impact was observed in the upper troposphere, it is encouraging to find a positive impact on the atmospheric layers more sensitive to surface radiation.

Furthermore, the expanded utilization of ATMS channels 8–15 over sea ice had an impact on the RMSD at levels above 300 hPa. The differences were below 0.5% and exhibited small significance, except for the levels above 10 hPa. Specifically, at the 10 hPa levels where the atmosphere is most sensitive to observations from ATMS channels 13–15, a significant decrease in RMSD was observed with significance levels exceeding 95%.

Additionally, the ensemble spreads (SPRD) of SeaIceEXP and CTRL were compared. The difference in ensemble spread between the experiments is shown in Fig. 10(b). The spread index was calculated using (10), but ZM_RMSD was replaced by the zonal mean of ensemble spread (ZM_SPRD). As a result of SeaIceEXP, ensemble spread decreased at all levels by up to 0.3% suggesting a reduction in the random error and an improvement in the reliability of the ensemble analysis results.

The RMSD index and the ensemble spreads for humidity were examined, but the impact was found to be insignificant except near the surface (not shown). However, the trend of both increasing and decreasing directions was consistent with those observed in the temperature fields. The limited impact on humidity fields can be attributed to the fact that in both experiments, the observations from humidity-sounding channels were not assimilated over sea ice. This study, therefore, primarily focuses on analyzing the impact of the developed bias correction scheme on atmospheric temperature fields.
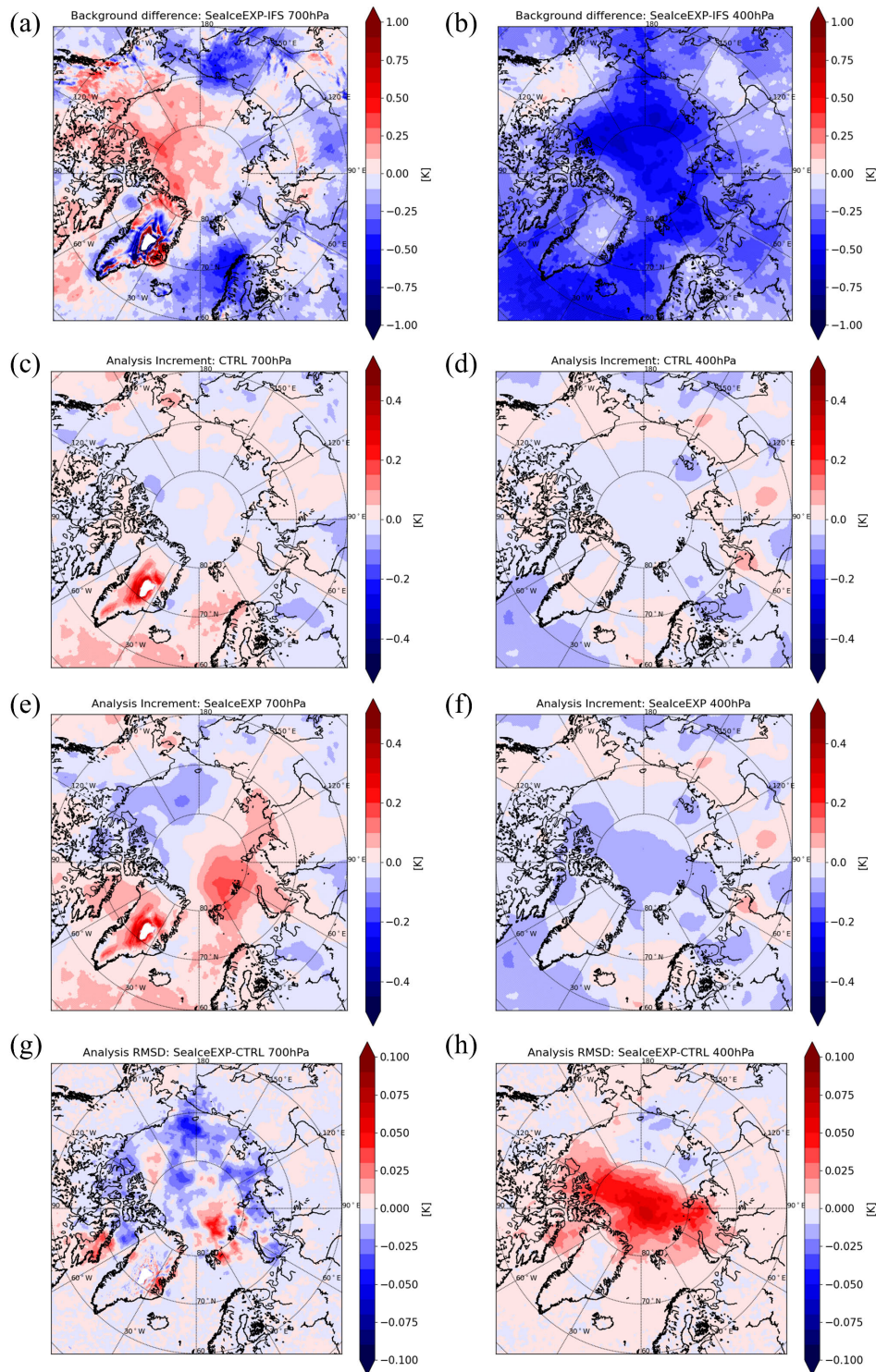
Fig. 11. The 45-day mean distribution of statistical analysis of temperature at (left column) 700 hPa and (right column) 400 hPa in kelvin unit. (a) and (b) Background difference between SeaIceEXP and ECMWF IFS. (c) and (d) Analysis increment of CTRL. (e) and (f) Analysis increment of SeaIceEXP. (g) and (h) Difference in analysis RMSD between SeaIceEXP and CTRL.

Furthermore, the analysis fields were evaluated against the ATMS and AMSU-A radiances. AMSU-A was utilized as evaluation data and the preprocessing method for AMSU-A was not investigated in this study. To make a comparison, the analysis fields from both experiments were used to simulate ATMS and AMSU-A radiances, and then the differences in

TBs between the observation and the simulation (hereafter, referred to as O−A) were examined. It should be noted that the observations before bias correction were used for the evaluation.

Fig. 12 shows the statistical analysis of O−As for AMSU-A channels assimilated in the KIM system together with the
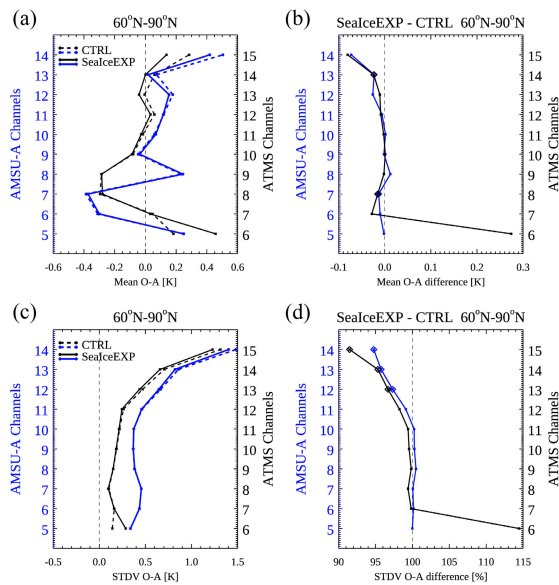
Fig. 12. Statistics of the analysis departures before bias correction for AMSU-A are shown in blue, while the statistics for AMSU-A equivalent ATMS channels are displayed in black. (Left column) Results for the CTRL with dashed lines and the SeaIceEXP with solid lines. (Right column) Difference between the two experiments (SeaIceEXP minus CTRL). The levels where the significance level is above 95% is represented by red diamond symbols. (Upper) (a) Mean bias and (b) difference in absolute mean bias. (Bottom) (c) Standard deviation and (d) normalized difference in standard deviation.

statistical analysis results for equivalent ATMS channels. In both CTRL and SeaIceEXP, AMSU-A channels 5–14 were assimilated in the ocean while in the sea, ice and channels 5 and 6 were not assimilated due to the problem with the simulation of surface radiance. At ATMS channel 6, the bias and standard deviation of O–A were larger in the SeaIceEXP than that of the CTRL due to the uncertainties in radiance simulation. However, after the bias correction, the analysis departure slightly decreased as a result of SeaIceEXP (not shown). At the AMSU-A channels 5 and 6, which have the same frequencies as ATMS channels 6 and 7, the effect was minimal because they were not assimilated over sea ice. Instead, the SeaIceEXP displayed a smaller mean bias and standard deviation of O−As compared to CTRL for the upper stratospheric AMSU-A channels (e.g., channels 12–14 which have the same frequencies as ATMS channels 13–15 and have the weighting function peaks above 10 hPa). The average bias decreased by up to 0.07 K, and the standard deviation decreased by approximately 5%. The effect on the stratospheric channels aligns with the reduction in temperature RMSD at above 10 hPa. These findings can be attributed to the increased utilization of sea ice observations, as well as the reduced bias and standard deviation in observation departures at the ATMS channels 13–15. The differences were negligible for the Microwave Humidity Sounder (MHS), suggesting a minor impact on humidity fields (not shown).

The impact on the forecast fields was generally negligible, with a difference of less than 0.5% (not shown) as the analysis change had a near-neutral effect. While there were slight increases in the 500 hPa geopotential height forecast from day 1 to day 5, and in the temperature forecast at levels below 500 hPa.

V. CONCLUSION

In this study, a preprocessing method was investigated to enhance the utilization of ATMS measurements over sea ice in the NWP model. Specifically, the proposed approach aimed to address the problem inherent in estimating the radiances emitted from the sea ice surface by utilizing the dynamically calculated sea ice emissivity and by correcting the bias between observation and background TBs.

The emissivity was dynamically derived using the ATMS observations and KIM forecasting data with the RTTOV model. The background TBs simulated using dynamic emissivities were found to be well-correlated with the ATMS observations. However, in winter sea ice areas, the simulated TB is negatively biased compared to the observations at channels 5 and 6. To minimize the bias and therefore to assimilate ATMS observations over sea ice, the sensitivities of microwave TBs to the contributing variables, such as surface temperature, emissivity, atmospheric upwelling/downwelling TBs, and atmospheric transmittance, were examined. It was revealed that the TBs at channels 5 and 6 were prone to be biased when the surface emissivity and/or surface temperature and/or upwelling TBs are uncertain, which indicates that the primary causes of the O–B are the discrepancies in these variables.

Accordingly, a multilinear regression equation was derived to estimate the O–B bias, by taking into account the uncertainties in surface emissivity, surface temperature, and atmospheric upwelling TB. The predictors that showed a linear relationship with the O–B were selected and the regression coefficients were computed using a 15-day dataset of ATMS observation and KIM 6-h forecasting data. The biases were effectively estimated using the selected predictors and regression coefficients with correlation coefficients of approximately 0.6. After bias correction, the biases in the TB difference between observation and simulation were decreased to 0.00 K at both ATMS channels 5 and 6.

Further, the assimilation experiment was conducted to analyze the impact of assimilating near-surface observations (i.e., ATMS channels 6 and 7) over winter sea ice, which are not utilized in the operational KIM system due to uncertainties in radiance simulation. The dynamic emissivity was used to simulate sea ice surface radiance at temperature channels and the selected bias predictors were used to correct the O–B bias at ATMS channel 6 over winter sea ice. The assimilation of additional sea ice observations had an impact on the temperature analysis fields. Specifically, the RMSD of temperature in layers from the surface to 500 hPa decreased against that of IFS, as a result of the assimilation of ATMS channel 6 observations. Furthermore, the RMSD decreased at levels above 10 hPa, indicating improvements in the quality and quantity of ATMS observations at the stratospheric channels that have been operationally used in the KIM. However, the RMSD of temperature in the layer from 500 to 300 hPa increased, influenced by the assimilation of ATMS channel 7 data. In addition, the analysis fields were evaluated against

AMSU-A radiance. Although the changes in RMSD were generally insignificant with a magnitude of less than 1% and large temporal variability, a noticeable improvement in analysis departures was observed at the uppermost AMSU-A channel, indicating that the reduction in RMSD at levels above 10 hPa is meaningful.

It is prospective to observe positive effects at the levels where the weighting function of ATMS channel 6 is distributed. Moreover, the preprocessing method proposed in this study expanded the availability of temperature information at all atmospheric levels in the Arctic Sea ice regions, without any significant negative impact on the analysis or forecast fields. Furthermore, our preliminary analysis suggests the applicability of this methodology to near-surface microwave observations over the Antarctic Sea ice. However, further investigation is still necessary to fully evaluate and optimize the proposed method. For instance, there is potential for exploring the use of Lambertian reflection, rather than specular reflection, particularly for the 50 and 183 GHz channels. Additionally, in an operational NWP system, the calculation of bias correction coefficients in real-time or adjustments would be necessary to accommodate the temporal variation of sea ice conditions. Furthermore, a cycling experiment would be required to fully evaluate the assimilation experiment and assess its effectiveness over multiple assimilation cycles.

REFERENCES

[1] S. English et al., "Impact of satellite data," ECMWF, Reading, U.K., Tech. Memorandum 711, 2013.

[2] S. Joo, J. Eyre, and R. Marriott, "The impact of MetOp and other satellite data within the met office global NWP system using an adjoint-based sensitivity method," *Monthly Weather Rev.*, vol. 141, no. 10, pp. 3331–3342, Oct. 2013.

[3] J. R. Eyre et al., "Assimilation of satellite data in numerical weather prediction. Part I: The early years," *Quart. J. Roy. Meteorolog. Soc.*, vol. 146, no. 726, pp. 49–68, 2020.

[4] N. C. Grody, "Surface identification using satellite microwave radiometers," *IEEE Trans. Geosci. Remote Sens.*, vol. 26, no. 6, pp. 850–859, Nov. 1988.

[5] S. J. English, "The importance of accurate skin temperature in assimilating radiances from satellite sounding instruments," *IEEE Trans. Geosci. Remote Sens.*, vol. 46, no. 2, pp. 403–408, Feb. 2008.

[6] F. T. Ulaby et al., *Microwave Radar and Radiometric Remote Sensing*, vol. 4, no. 5. Ann Arbor, MI, USA: Univ. Michigan Press, 2014, p. 6.

[7] N. T. Kurtz and T. Markus, "Satellite observations of Antarctic sea ice thickness and volume," *J. Geophys. Res., Oceans*, vol. 117, no. C8, Aug. 2012, Art. no. C08025.

[8] F. J. Turk, L. Li, and Z. S. Haddad, "A physically based soil moisture and microwave emissivity data set for global precipitation measurement (GPM) applications," *IEEE Trans. Geosci. Remote Sens.*, vol. 52, no. 12, pp. 7637–7650, Dec. 2014.

[9] S. Lee, H. Shi, B. Sohn, A. J. Gasiewski, W. N. Meier, and G. Dybkjær, "Winter snow depth on Arctic sea ice from satellite radiometer measurements (2003–2020): Regional patterns and trends," *Geophys. Res. Lett.*, vol. 48, no. 15, Aug. 2021, Art. no. GL094541.

[10] C. Prigent, J.-P. Wigneron, W. B. Rossow, and J. R. Pardo-Carrion, "Frequency and angular variations of land surface microwave emissivities: Can we estimate SSM/T and AMSU emissivities from SSM/I emissivities?" *IEEE Trans. Geosci. Remote Sens.*, vol. 38, no. 5, pp. 2373–2386, 2000.

[11] F. Weng, B. Yan, and N. C. Grody, "A microwave land emissivity model," *J. Geophys. Res., Atmos.*, vol. 106, no. D17, pp. 20115–20123, Sep. 2001.

[12] J. R. Eyre et al., "Assimilation of satellite data in numerical weather prediction. Part II: Recent years," *Quart. J. Roy. Meteorolog. Soc.*, vol. 148, no. 743, pp. 521–556, Jan. 2022.

[13] S. Lee, B. Sohn, and S. Kim, "Differentiating between first-year and multiyear sea ice in the Arctic using microwave-retrieved ice emissivities," *J. Geophys. Res., Atmos.*, vol. 122, no. 10, pp. 5097–5112, May 2017.

[14] C. Prigent, W. B. Rossow, and E. Matthews, "Microwave land surface emissivities estimated from SSM/I observations," *J. Geophys. Res., Atmos.*, vol. 102, no. D18, pp. 21867–21890, Sep. 1997.

[15] F. Karbou, C. Prigent, L. Eymard, and J. R. Pardo, "Microwave land emissivity calculations using AMSU measurements," *IEEE Trans. Geosci. Remote Sens.*, vol. 43, no. 5, pp. 948–959, May 2005.

[16] F. Karbou, É. Gérard, and F. Rabier, "Microwave land emissivity and skin temperature for AMSU-A and -B assimilation over land," *Quart. J. Roy. Meteorolog. Soc.*, vol. 132, no. 620, pp. 2333–2355, Oct. 2006.

[17] N. Mathew, G. Heygster, C. Melsheimer, and L. Kaleschke, "Surface emissivity of Arctic sea ice at AMSU window frequencies," *IEEE Trans. Geosci. Remote Sens.*, vol. 46, no. 8, pp. 2298–2306, Aug. 2008.

[18] N. Mathew, G. Heygster, and C. Melsheimer, "Surface emissivity of the Arctic sea ice at AMSR-E frequencies," *IEEE Trans. Geosci. Remote Sens.*, vol. 47, no. 12, pp. 4115–4124, Dec. 2009.

[19] S. Guedj, F. Karbou, F. Rabier, and A. Bouchard, "Toward a better modeling of surface emissivity to improve AMSU data assimilation over Antarctica," *IEEE Trans. Geosci. Remote Sens.*, vol. 48, no. 4, pp. 1976–1985, Apr. 2010.

[20] J.-L. Moncet et al., "Land surface microwave emissivities derived from AMSR-E and MODIS measurements with advanced quality control," *J. Geophys. Res.*, vol. 116, no. D16, 2011, Art. no. D16104.

[21] F. Karbou, E. Gérard, and F. Rabier, "Global 4DVAR assimilation and forecast experiments using AMSU observations over land. Part I: Impacts of various land surface emissivity parameterizations," *Weather Forecasting*, vol. 25, no. 1, pp. 5–19, Feb. 2010.

[22] F. Karbou, F. Rabier, and C. Prigent, "The assimilation of observations from the advanced microwave sounding unit over sea ice in the French global numerical weather prediction system," *Monthly Weather Rev.*, vol. 142, no. 1, pp. 125–140, Jan. 2014.

[23] R. T. Tonboe, G. Dybkjær, and J. L. Høyer, "Simulations of the snow covered sea ice surface temperature and microwave effective temperature," *Tellus A, Dyn. Meteorol. Oceanogr.*, vol. 63, no. 5, p. 1028, Jan. 2011.

[24] A. Bouchard, F. Rabier, V. Guidard, and F. Karbou, "Enhancements of satellite data assimilation over Antarctica," *Monthly Weather Rev.*, vol. 138, no. 6, pp. 2149–2173, Jun. 2010.

[25] N. Bormann et al., "Assessment of the forecast impact of surface sensitive microwave raidnaces over land and sea ice," ECMWF, Reading, U.K., Tech. Memorandum 804, 2017.

[26] E. Di Tomaso and N. Bormann, "Assimilation of ATOVS radiances at ECMWF, second year EUMETSAT fellowship report," EUMETSAT, Darmstadt, Germany, Res. Rep. 25, 2012.

[27] H. Lawrence, N. Bormann, I. Sandu, J. Day, J. Farnan, and P. Bauer, "Use and impact of Arctic observations in the ECMWF numerical weather prediction system," *Quart. J. Roy. Meteorolog. Soc.*, vol. 145, no. 725, pp. 3432–3454, Oct. 2019.

[28] R. T. Tonboe, "The simulated sea ice thermal microwave emission at window and sounding frequencies," *Tellus A*, vol. 62, no. 3, pp. 333–344, May 2010.

[29] S. Lee and B. Sohn, "Retrieving the refractive index, emissivity, and surface temperature of polar sea ice from 6.9 GHz microwave measurements: A theoretical development," *J. Geophys. Res., Atmos.*, vol. 120, no. 6, pp. 2293–2305, Mar. 2015.

[30] L. Kilic, R. T. Tonboe, C. Prigent, and G. Heygster, "Estimating the snow depth, the snow–ice interface temperature, and the effective temperature of Arctic sea ice using advanced microwave scanning radiometer 2 and ice mass balance buoy data," *Cryosphere*, vol. 13, no. 4, pp. 1283–1296, Apr. 2019.

[31] R. H. Reichle, "Data assimilation methods in the Earth sciences," *Adv. Water Resour.*, vol. 31, no. 11, pp. 1411–1418, Nov. 2008.

[32] C.-H. Lyu, E. J. Kim, L. M. Mccormick, R. V. Leslie, and I. A. Osaretin, "JPSS-1 ATMS postlaunch active geolocation analysis," *IEEE Trans. Geosci. Remote Sens.*, vol. 59, no. 11, pp. 9462–9471, Nov. 2021.

[33] E. Kim, C. J. Lyu, K. Anderson, R. V. Leslie, and W. J. Blackwell, "S-NPP ATMS instrument prelaunch and on-orbit performance evaluation," *J. Geophys. Res., Atmos.*, vol. 119, no. 9, pp. 5653–5670, May 2014.

[34] F. Weng et al., "Calibration of Suomi National Polar-Orbiting Partnership Advanced Technology Microwave Sounder," *J. Geophys. Res., Atmos.*, vol. 118, no. 19, pp. 11–187, Oct. 2013.

[35] N. Grody, J. Zhao, R. Ferraro, F. Weng, and R. Boers, "Determination of precipitable water and cloud liquid water over oceans from the NOAA 15 advanced microwave sounding unit," *J. Geophys. Res., Atmos.*, vol. 106, no. D3, pp. 2943–2953, Feb. 2001.

[36] R. Bennartz, A. Thoss, A. Dybbroe, and D. B. Michelson, "Precipitation analysis using the advanced microwave sounding unit in support of nowcasting applications," *Meteorolog. Appl.*, vol. 9, no. 2, pp. 177–189, Jun. 2002.

[37] S.-Y. Hong et al., "The Korean integrated model (KIM) system for global weather forecasting," *Asia–Pacific J. Atmos. Sci.*, vol. 54, no. S1, pp. 267–292, Jun. 2018.

[38] E. Kalnay, *Atmospheric Modeling, Data Assimilation and PreDictability*. Cambridge, U.K.: Cambridge Univ. Press, 2003.

[39] B. R. Hunt et al., "Efficient data assimilation for spatiotemporal chaos: A local ensemble transform Kalman filter," *Phys. D, Nonlinear Phenom.*, vol. 230, nos. 1–2, pp. 112–126, 2007.

[40] I.-H. Kwon et al., "Development of an operational hybrid data assimilation system at KIAPS," *Asia–Pacific J. Atmos. Sci.*, vol. 54, no. S1, pp. 319–335, Jun. 2018.

[41] J.-H. Kang et al., "Development of an observation processing package for data assimilation in KIAPS," *Asia–Pacific J. Atmos. Sci.*, vol. 54, no. S1, pp. 303–318, Jun. 2018.

[42] J. Hocking et al., "RTTOV v10 users guide," EUMETSAT, Darmstadt, Germany, Tech. Rep. NWPSAF-MO-UD-0123, 2012.

[43] C. J. Donlon, M. Martin, J. Stark, J. Roberts-Jones, E. Fiedler, and W. Wimmer, "The operational sea surface temperature and sea ice analysis (OSTIA) system," *Remote Sens. Environ.*, vol. 116, pp. 140–158, Jan. 2012.

[44] T. Haiden et al., *Evaluation of ECMWF Forecasts, Including the 2018 Upgrade*. Reading, U.K.: European Centre for Medium-Range Weather Forecasts, 2018.

[45] M. D. Goldberg, D. S. Crosby, and L. Zhou, "The limb adjustment of AMSU—A observations: Methodology and validation," *J. Appl. Meteorol.*, vol. 40, no. 1, pp. 70–83, Jan. 2001.

[46] R. C. Harlow, "Millimeter microwave emissivities and effective temperatures of snow-covered surfaces: Evidence for Lambertian surface scattering," *IEEE Trans. Geosci. Remote Sens.*, vol. 47, no. 7, pp. 1957–1970, Jul. 2009.

[47] N. Bormann, "Accounting for Lambertian reflection in the assimilation of microwave sounding radiances over snow and sea-ice," *Quart. J. Roy. Meteorolog. Soc.*, vol. 148, no. 747, pp. 2796–2813, Jul. 2022.

[48] J. H. Jiang and D. L. Wu, "Ice and water permittivities for millimeter and sub-millimeter remote sensing applications," *Atmos. Sci. Lett.*, vol. 5, no. 7, pp. 146–151, Oct. 2004.

[49] R. T. Tonboe, H. Schyberg, E. Nielsen, K. R. Larsen, and F. T. Tveter, "The EUMETSAT OSI SAF near 50 GHz sea ice emissivity model," *Tellus A, Dyn. Meteorol. Oceanogr.*, vol. 65, no. 1, Dec. 2013, Art. no. 18380.

[50] J. C. Comiso, "Characteristics of Arctic winter sea ice from satellite multispectral microwave observations," *J. Geophys. Res., Oceans*, vol. 91, no. C1, pp. 975–994, Jan. 1986.

[51] J. C. Comiso, T. C. Grenfell, D. L. Bell, M. A. Lange, and S. F. Ackley, "Passive microwave in situ observations of winter Weddell sea ice," *J. Geophys. Res., Oceans*, vol. 94, no. C8, pp. 10891–10905, Aug. 1989.

[52] R. Saunders et al., "An update on the RTTOV fast radiative transfer model (currently at version 12)," *Geosci. Model Develop.*, vol. 11, no. 7, pp. 2717–2737, Jul. 2018.

[53] J. I. Daoud, "Multicollinearity and regression analysis," *J. Phys., Conf. Ser.*, vol. 949, Dec. 2017, Art. no. 012009.

[54] A. Kraha, H. Turner, K. Nimon, L. R. Zientek, and R. K. Henson, "Tools to support interpreting multiple regression in the face of multicollinearity," *Frontiers Psychol.*, vol. 3, p. 44, Mar. 2012.

[55] B. Harris and G. Kelly, "A satellite radiance-bias correction scheme for data assimilation," *Quart. J. Roy. Meteorolog. Soc.*, vol. 127, no. 574, pp. 1453–1468, Apr. 2001.

[56] A. Persson and F. Grazzini, "User guide to ECMWF forecast products," *Meteorolog. Bull.*, vol. 3, no. 2, pp. 1–161, 2007.

Ji-Soo Kim received the B.S. degree in environmental engineering and the M.S. degree in atmospheric science and engineering from Ewha Womans University, Seoul, South Korea, in 2016 and 2018, respectively, where she is currently pursuing the Ph.D. degree.

Her research interests include preprocessing techniques of microwave observation, including estimation of surface radiance, bias correction, and cloud screening for numerical weather prediction systems.

Myoung-Hwan Ahn received the B.S. degree in atmospheric sciences from Seoul National University, Seoul, South Korea, in 1987, and the Ph.D. degree in meteorology from the University of Maryland at College Park, College Park, MD, USA, in 1997. His doctoral thesis focuses on the development of an algorithm to retrieve SO2 from the TOMS instrument onboard the Nimbus-7 satellite.

Before joining, Ewha Womans University, Seoul, as a Professor, in 2012, he worked for the Korea Meteorological Administration (KMA), Seoul, as a Senior Researcher. During his career at KMA, he led a group of scientists to develop the level 2 data processing system of the meteorological imager onboard a multipurpose geostationary satellite which is the first Korean Meteorological Satellite. After the successful commissioning of the first satellite and related data processing system, he laid out the follow-on GK-2 satellite program before moving to the university. His research interests include centered around the GK-2 program including instrument characterization, retrieval theory, and information content for the atmospheric profiles which are closely related to the retrieval algorithm for the advanced meteorological imager of GK-2 satellite, as well as cloud detection using ground-based passive instruments such as the infrared thermometer, and utilization of remote sensing data for the numerical weather prediction model.

Sang-Moo Lee (Member, IEEE) received the B.S. and Ph.D. degrees in earth environmental science from Seoul National University, Seoul, South Korea, in 2011 and 2018, respectively.

In 2019, he was an Assistant Research Professor of Brain Korea 21 Plus Project with Seoul National University. From 2019 to 2022, he joined as a Post-Doctoral Research Fellow with the Center for Environmental Technology, Department of Electrical, Computer, and Energy Engineering, University of Colorado Boulder (CU), Boulder, CO, USA, where he was a Visiting Scholar with the National Snow and Ice Data Center, Cooperative Institute for Research in Environmental Sciences. He is currently an Assistant Professor with the School of Earth and Environmental Sciences, Seoul National University. His research interests include atmospheric radiation, radiative transfer modeling, and remote sensing.